12-1-2014

Retrieval of Spectral Reflectance of High Resolution Multispectral Imagery Acquired with an Autonomous Unmanned Aerial Vehicle: AggieAir™

Bushra Zaman
Utah State University, bzaman27@gmail.com

Austin Jensen
Utah State University

Shannon R. Clemens
Utah State University

Mac McKee
Utah State University

Retrieval of Spectral Reflectance of High Resolution Multispectral Imagery Acquired with an Autonomous Unmanned Aerial Vehicle: AggieAir™

Bushra Zaman, Austin Jensen, Shannon R. Clemens, and Mac McKee

Abstract

This research presents a new semi-automatic model for converting raw AggieAir™ footprints in visible and near-infrared (NIR) bands into reflectance images. AggieAir, a new unmanned aerial vehicle (UAV) platform, is flown autonomously using pre-programmed flight plans at low altitudes to limit atmospheric effects. The UAV acquires high-resolution, multispectral images and has a flight interval of about 30 minutes. The sensors on board are twin cameras with duplicate settings and automatic mode disabled. A white Barium Sulfate (BaSO4) panel is used for reflectance calibration and in situ irradiance measurements. The spatial and radiometric resolution of the imagery is 25 cm and 8-bit, respectively. The raw images are mosaicked and orthorectified and the model converts their digital numbers (DN) to reflectance values. Imagery, acquired around local solar noon over wetlands on the Great Salt Lake, Utah, is used to illustrate the results. The model generates high quality images and the results are good. The reflectance values of vegetation in the NIR, Green and Red bands extracted at the test locations are consistent. The image processing, reflectance calculations, accuracy issues, with the proposed method are discussed.

Introduction

In the recent past, various unmanned aerial vehicle (UAV) platforms equipped with a myriad of devices have been used to gather data in different bands for an array of applications. It is an area of remote sensing that has become very active, and UAVs are rapidly becoming the preferred platform for development of remote sensing applications (Watts *et al.,* 2012). Earth orbiting satellites and manned aircraft remote sensors have the advantage of covering large areas, but the high operating cost of such instruments limits the availability of timely information for specific areas of interest (Hakala *et al*., 2010). Remote sensing applications require more sustainable, affordable, user-friendly systems which are compliant with various levels of changes in technology. Zhang and Kovacs (2012) state that low altitude remote sensing platforms, or UAVs address most of these issues, and can be a potential alternative to satellite imagery given their low cost of operation, high spatial and temporal resolution, and flexibility in image acquisition programming. UAV imagery provides the ability to quantify spatial patterns, and is used in rangeland monitoring and mapping to quantify patches of vegetation and soil not detectable with piloted aircraft or satellite imagery (Laliberte and Rango, 2009). UAV data have been extensively used in forest fire applications (Merino *et al*., 2006, Ambrosia *et al*., 2003), wetland management and riparian applications (Zaman *et al.,* 2011, Jensen *et al*., 2011), precision agriculture (Primicerio *et al*., 2012), agricultural decision support (Herwitz *et al*., 2004). Field reflectance data from UAV platforms are also increasingly being used for image classification and predictive models (Berni *et al*., 2009). But the accuracy issues related with conversion of the information acquired by the sensors on board these UAVs into useful data remains a widely discussed topic. The small UAV systems have low payload capabilities and are commonly equipped with lightweight, low-cost digital cameras, which may complicate the image processing procedures. Additionally, the chemical basis for making a filter used on these cameras is proprietary and there is variation in filter spectral transmittances among various digital cameras (Hunt *et al*., 2010), which calls for a specific radiometric and geometric calibration (Hruska *et al.,* 2012) to produce reliable data. Several UAV imaging systems require custom designed applications for photogrammetric processing and creation of orthomosaics to handle the large number of small-footprint images acquired by the UAVs with a rather unstable platform (Du *et al.,* 2008; Laliberte and Rango, 2008; Wilkinson *et al*., 2009). This paper discusses processing of data obtained from a brand new UAV system, AggieAir™, which uses off-the-shelf Canon PowerShot SX100 cameras as sensors.

UAV imagery has spectral information in the form of digital numbers which have noises arising from changing view, illumination geometry, and instrument errors. Huang *et al*., 2002 demonstrate the necessity of converting DN to at-satellite reflectance when atmospheric correction is not feasible. DN is a function not only of land-cover, but also of the sensor calibration, solar zenith angle, sensor viewing angle, seasonally variable Earth/Sun distance, and diurnally variable atmospheric conditions (Slater, 1980). Exposure settings on the digital camera are chosen based on overall light intensity, which varies over time with changes in solar elevation, atmospheric transmittance, and clouds (Gates, 2003). Consequently, it is desirable to convert DN to reflectance values that corrects for these changes (Hunt *et al*., 2005). Surface reflectance value has become the vital measurement required for most remote sensing models (Moran *et al*., 2001). Laliberte *et al.* (2011) state that a UAS-based image acquisition system produces hundreds of very high resolution small footprint images that require geometric and radiometric corrections and subsequent mosaicking for use in a Geographic Information System (GIS) and extraction of meaningful data. Similarly Jensen *et al.* (2010) discuss the necessity of calibration of UAV imagery and navigation sensors.

UWRL 247, Utah Water Research Laboratory, College of Engineering. 1600 East Canyon Road, Logan, UT 84321 (b.zaman@aggiemail.usu.edu).

Photogrammetric Engineering & Remote Sensing
Vol. 80, No. 12, December 2014, pp. 1139–1150.
0099-1112/14/8012–1139

doi: 10.14358/PERS.80.12.1139

This paper discusses the model created to process the data acquired by a new UAV platform, AggieAir, descriptions of its sensors, technique used for DN to reflectance conversion, cross-calibration of white Barium Sulfate ($BaSO_4$) reference panel used for recording *in situ* solar irradiance, and accuracy issues encountered in the process.

Study Area

The Bear River Migratory Bird Refuge (BRMBR), at 41°28'45.43"N 112°16'00.81"W, elevation 1,284 m, is located on the northeast shore of the Great Salt Lake, Utah, at the terminus of the Bear River. Figure 1 shows a section of the BRMBR, about 11 km^2 which is used to illustrate the results of this study. The BRMBR, managed by the US Fish and Wildlife Service as part of the National Wildlife Refuge System, comprises over 300 square kilometers of marsh, open water, uplands, and alkali mudflats, and is one of the largest wetland complexes along the Great Salt Lake. With its location and size, the BRMBR provides critical wetlands wildlife habitat and resting grounds for migratory birds along the Pacific Flyway. It is one of the most important habitat areas for migratory birds in North America. As part of the Bear River Bay, the Refuge is designated as a Western Hemisphere Shorebird Reserve Network site, a globally important shorebird area.

Data Acquisition

The AggieAir

AggieAir Flying Circus is a service center at the Utah Water Research Laboratory which provides high-resolution, multispectral aerial imagery using a small, unmanned aerial system called AggieAir. The UAV aircraft has 1.2 m (4 ft) to 2.4 m (8 ft) wingspans, is approximately 3.6 kg (8 lbs), and is equipped with computer, avionics, global positioning system (GPS), radio control (RC), flight control, and payload management software (Figure 2). AggieAir platform is battery powered, fully autonomous or RC, easy to use with a speed of approximately 50 km/h (30 mph). The distance covered by the UAV is approximately 50 km (30 mph) per battery charge. No runway is needed for its operation and is coven-capable. The data is

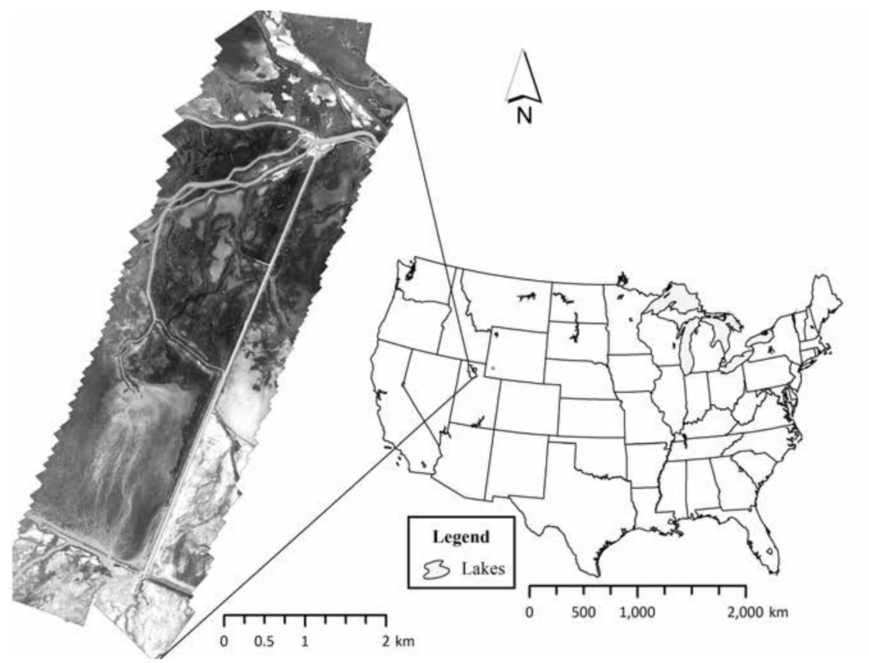

Figure 1. Study area.

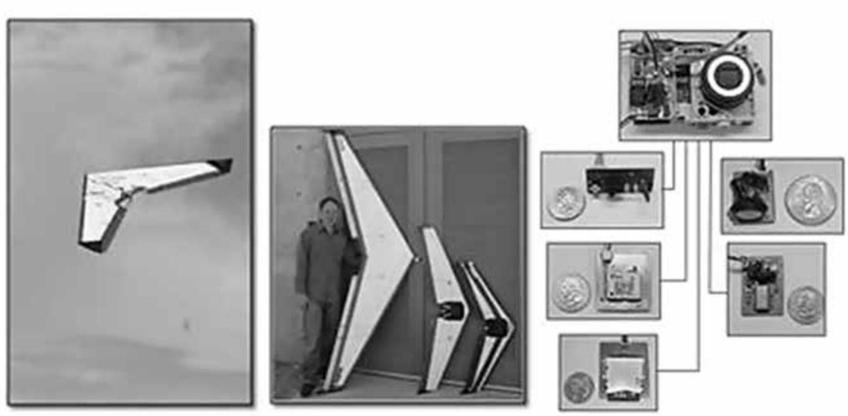

Figure 2. Components of AggieAir™ UAV.

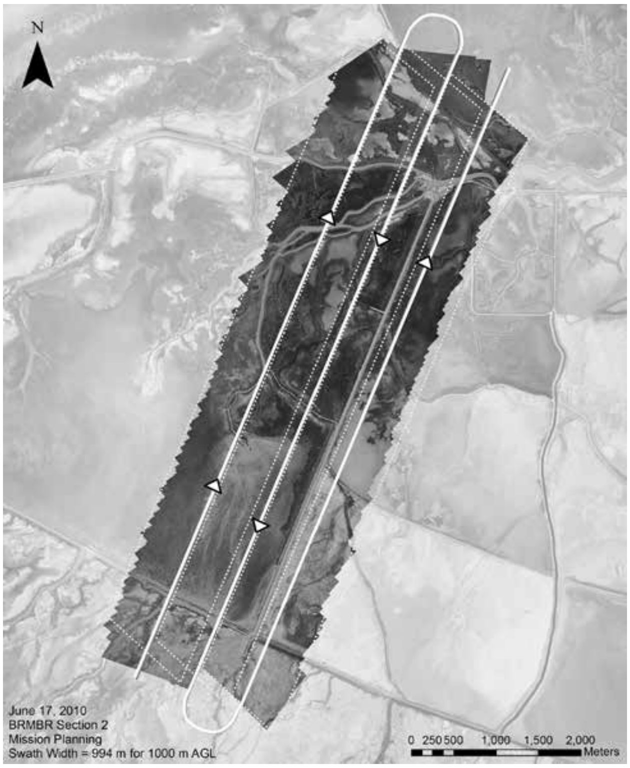

Figure 3. Flight plan of AggieAir™ UAV.

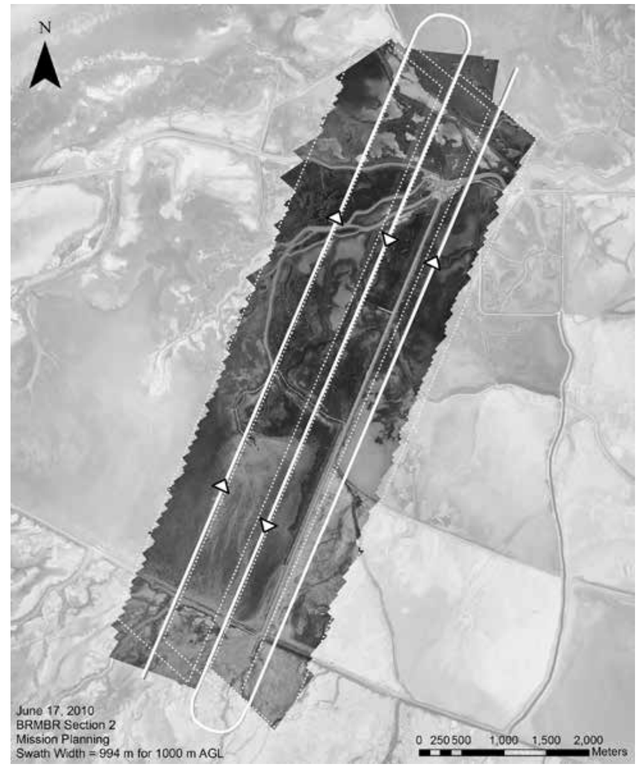

Figure 4. Raw image tiles projected on a basemap.

acquired in the visual and near-infrared (NIR) channels. The AggieAir platform is also equipped with thermal infrared (TIR) image acquisition capability and details about the TIR system, calibration, and applications have been discussed in detail by Sheng *et al.,* 2010.

The spatial resolution of the AggieAir images in the Visible and NIR bands varies from 5 cm to 25 cm, depending on flight elevation with fast turnaround of images (minutes to hours). AggieAir maps small areas quicker, more frequently, at finer resolution, and at a smaller cost than conventional remote sensing platforms (satellite and manned aircraft) (Jensen *et al.,* 2009). The cost of an inertial measurement unit (IMU) which accounts for a large portion of the total cost of an unmanned autonomous system lies somewhere between $500 USD to $3000 USD for industrial grade and costs less than $500 USD for hobbyist grade (Chao *et al.,* 2010). This lowers the total cost of the UAV as compared to satellite or manned aircrafts. Furthermore, AggieAir is independent of a runway, which gives the user the ability to launch the aircraft from virtually anywhere. For this mission, the aircraft was programmed with a flight plan and the study area was divided into three strips which were covered through the flightlines shown in Figure 3.

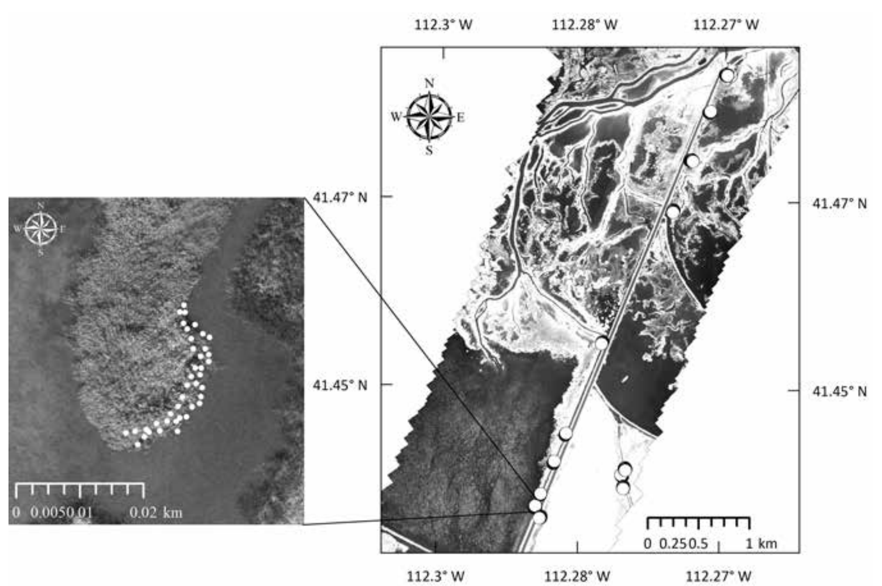

Figure 5. Ground reference sampling locations.

Data

The raw imagery from the UAV is in the JPEG format. Figure 4 shows raw image tiles from AggieAir.

At BRMBR, the ground reference data was only available for vegetative growth of an invasive plant species *Phragmites Australis*. The sampling was done as a part of a project which was carried out to help managers at the BRMBR and researchers at USU to map and monitor this invasive weed. A total of 12 Phragmites patches were identified in the study area for collecting field data, and the data was recorded to sample intensively for assessment of spread of this weed. The ground reference sampling locations are shown in Figure 5.

Sensors

The instrument used by AggieAir is a RGB digital camera, Canon PowerShot SX100, which has a 9-megapixel CCD sensor and an ISO range from 80 to 1600 and the digital imaging core (DIGIC) III processor. The radiometric resolution of the camera is 8-bit. The color filter array (CFA) configuration of Canon PowerShot

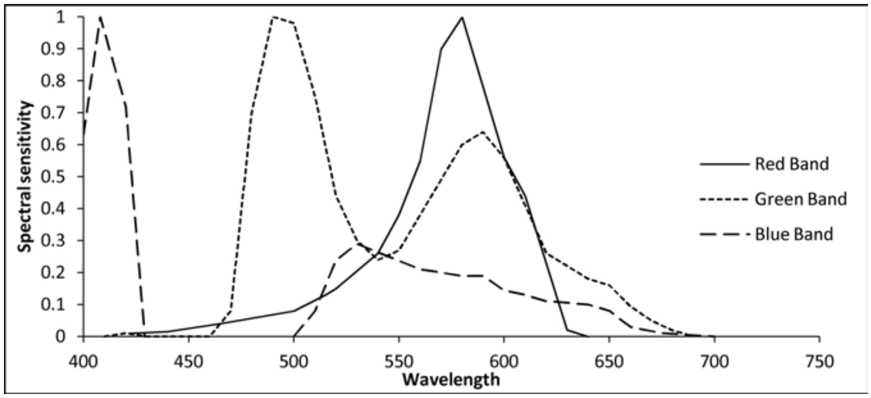

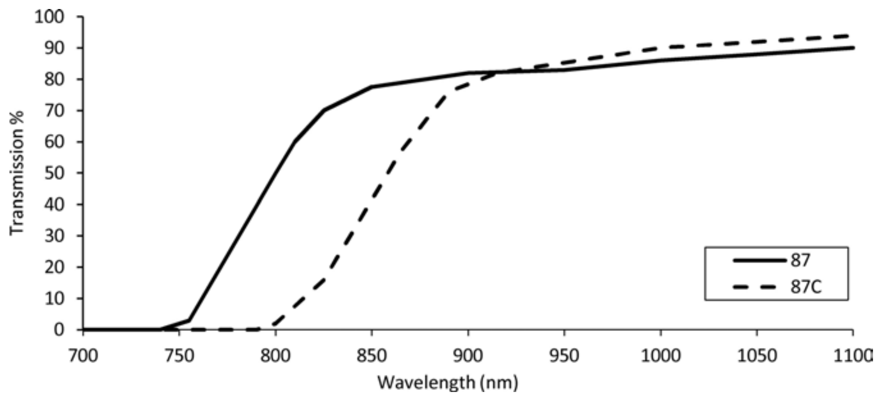

Figure 6. (a) Spectral response of the RGB camera Canon PowerShot SX100 for Red, Green and Blue channels, and (b)Transmission curve of NIR camera after deploying NIR Wratten 87 and 87C filters.

SX100 is the Bayer filter which has twice as many green pixels as red or blue. The filter permits only one color to be measured at each pixel (Red, Blue, or Green, and sometimes Cyan), and to create the color image, the missing color values are estimated for each pixel by means of CFA interpolation (Lebourgeois *et al.,* 2008). The automatic settings mode in the camera is disabled and it records an image size of 3,264 × 2,248 pixels at a time interval of 4 seconds, a 6 mm focal length with a field of view of 50 × 39 degrees. The camera weighs 250 grams.

The spectral response curves of the RGB camera for the red, Green and Blue channels are shown in Figure 6a. The NIR camera is also a Canon PowerShot SX100 with similar specifications, but with a RGB bandpass filter removed and replaced with a Wratten 87 NIR filter. The Wratten 87 NIR filter allows NIR wavelengths to pass through but not visible frequencies and blocks any wavelength below 740 nm and similarly the Wratten 87C NIR filter blocks all wavelengths below 790 nm as shown in Figure 6b.

Image Mosaicking & Ortho-rectification

EnsoMosaic UAV is a software (Mosaic Mill of Finland, LTD) which applies photogrammetric principles, in contrast to image stitching, to rectify images into orthomosaics and orthoimages. Orthomosaics and orthoimages are free of distortion for areas with elevation changes. Using aerial imagery acquired by AggieAir, a GPS log file of coordinates for each image, and exterior orientation information from on-board cameras, a Bundle Block Adjustment (BBA) is applied for automatic image rectification. BBA calculates location and orientation of the camera for every image to enable image rectification into a ground coordinate system. The output is an orthorectified mosaic (Figure 7) or individual images with a digital elevation model (DEM).

Spectral Reflectance Retrieval of AggieAir Imagery – Conversion of DN to Reflectance Value

Background

The reflectance factor is defined as the ratio of the radiant flux reflected by a surface to that reflected into the same reflected-beam geometry by an ideal (lossless), perfectly diffuse (Lambertian) standard surface irradiated under the same conditions (Nicodemus *et al.,* 1977). Reflectance is an appropriate and useful optical property for remote sensing field research because it is a fundamental property of the land-cover (Robinson and Biehl, 1979). To calculate reflectance of the UAV image the amount of incoming solar irradiance on that day and time frame needed to be quantified and a reference panel was used to get this information. In this research, processing and calibration methods were developed for use with a 0.6 m × 0.6 m white $BaSO_4$ panel that has a reflectance of 95 to 98percent (Labsphere, Inc., North Sutton, New Hampshire). The coefficients and subsequent spectral reflectance of the $BaSO_4$ panel were calculated using cross-calibration procedure. An Exotech radiometer with four bands matching the Landsat Thematic Mapper bands, TM1 (0.45-0.52 µm), TM2 (0.52-0.60 µm), TM3 (0.63-0.69 µm), and TM4 (0.76-0.90 µm), was used to record readings over the panels. The cross-calibration procedure is described in detail in the following section.

The RGB and NIR digital cameras on board the UAV were used for measuring radiance in the field. The reflectance factor for the unknown target, R_T, is determined using a modified reflectance mode method (Miura and Huete, 2009). The original

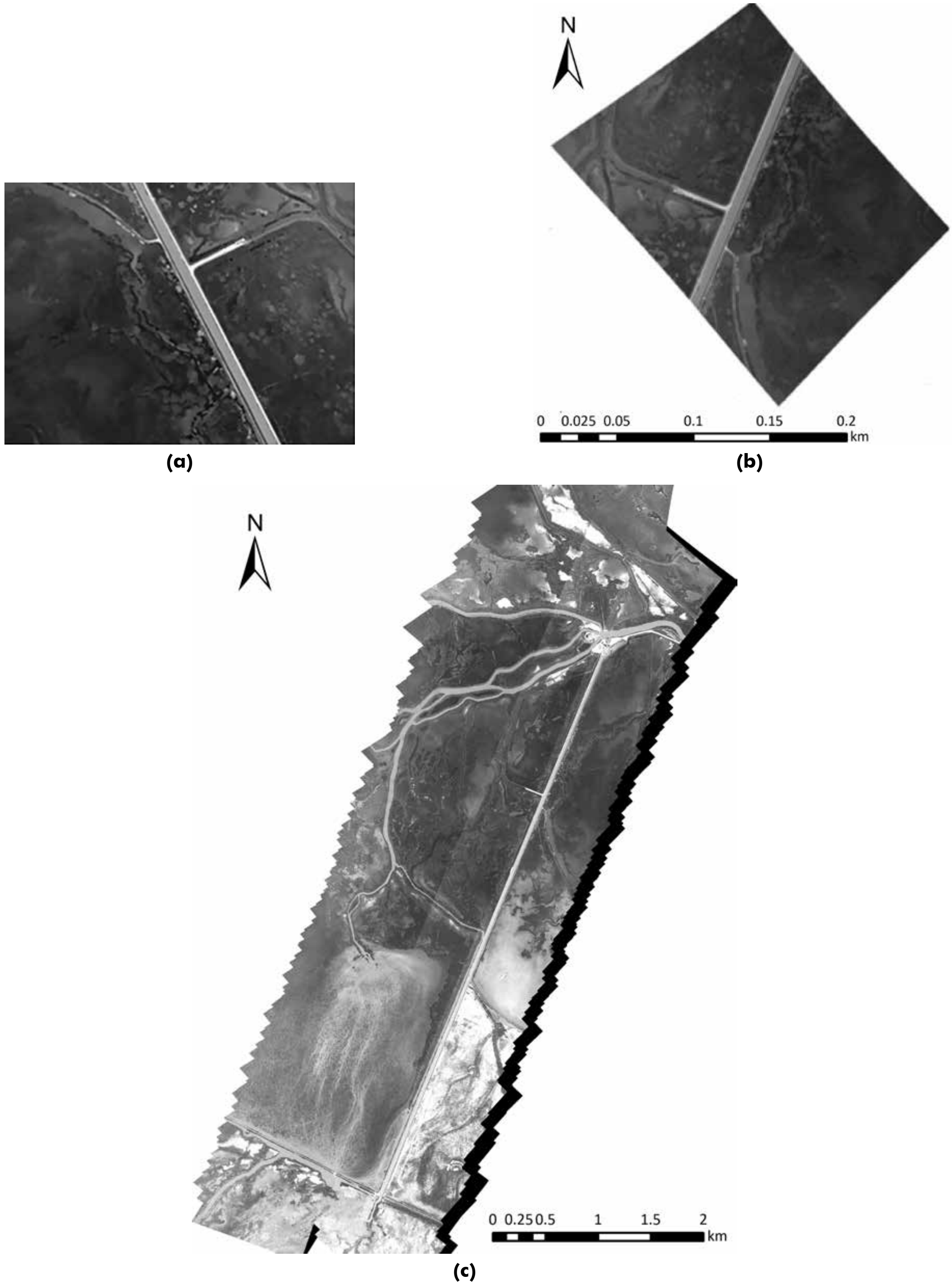

Figure 7. (a) Raw tile from UAV image acquisition, (b) Orthorectified tile, and (c) Orthorectified and mosaicked image.

"reflectance mode" method from Miura and Huete (2009) used a before-flight white panel reading using a spectrometer which was then mounted on-board a UAV. The results of the spectral reflectance retrievals were biased and got affected by the time of day and the length of the flight. This paper introduces a modification to this method by adding an after-flight white panel photo captured in the field using the same camera that was on-board the UAV. An average of the before and after flight data is used in the reflectance conversion which assumes a linearity due to the short duration of the flight (30 minutes). The modification is aimed at reducing the bias in the reflectance value conversion. The final white reference panel image, ($DN_R(t)$), used in calculations is the average of the DN of panel image taken before (t_0) and after the flight (t_1).

The spectral reflectance calculations of UAV imagery in the Red, Green, and NIR bands are done using Equation 1. The blue wavelengths undergo substantial attenuation by atmospheric scattering, and are thus left out in the calculations.

$$R_T(\theta_z) = \frac{DN_T(t)}{DN_R(t)} R_{BaSO_4}(0°/\theta_z) \quad (1)$$

where R_T is the reflectance factor of an unknown target; θ_z is the solar zenith angle at any time *t* with the radiometer/camera optical axis parallel to the surface normal (i.e., nadir-looking geometry); $DN_T(t)$ is the digital image array from the UAV when the instrument is viewing the target; $DN_R(t) = [DN_R(t_0)+DN_R(t_1)]/2$ is the digital image array of the white reference panel when the camera is viewing the reference panel at time t_0 and t_1; and $R_{BaSO4}(0°/\theta_z)$ is the reflectance factor of $BaSO_4$ panel at 0° view angle and sun zenith angle of θ_z.

The following sections describe the procedure for calculation of different components of Equation 1, i.e., $R_{BaSO4}(0°/\theta_z)$, $DN_R(t)$, $DN_T(t)$.

Calculation of Reflectance of White Reference Panel, $R_{BaSO4}(0°/\theta_z)$

The following equation is used for calculating the reflectance factor of the $BaSO_4$ panel:

$$R_{BaSO_4}(0°/\theta_z) = R_{Halon}(0°/\theta_z) \times \frac{V_{BaSO_4}}{V_{Halon}} \quad (2)$$

where $R_{BaSO4}(0°/\theta_z)$ = Reflectance factor of $BaSO_4$ panel at 0° view angle and sun zenith angle of θz, $R_{Halon}(0°/\theta_z)$ = Reflectance factor of Halon panel at 0° view angle and sun zenith angle of θz,

V_{BaSO4} = Voltage reading of the radiometer over the $BaSO_4$ panel, and V_{Halon} = Voltage reading of the radiometer over the Halon Panel.

Cross-calibration of $BaSO_4$ Panel with Halon Panel to Obtain Bi-directional Reflectance Coefficients

To obtain the coefficients of the barium sulfate ($BaSO_4$) panel, it was cross calibrated with respect to a Halon (polytetrafluoroethylene-based material) panel with known coefficients listed in Table 1 below.

Table 1. Bi-directional Reflectance Coefficients of Halon Panel

Halon Panel	(Jackson et al. (1992) RemSens.Env.				
	A0	A1	A2	A3	A4
Green	1.06E+00	7.11E-04	-9.72E-05	1.79E-06	-1.40E-08
Red	1.06E+00	7.55E-04	-1.02E-04	1.90E-06	-1.47E-08
NIR	1.06E+00	9.02E-04	-1.10E-04	2.05E-06	-1.56E-08

The calibration was done in an open field where the obstruction to light was a minimum and the source of diffuse irradiance was the hemispherical sky above the panel. The panels were placed in close proximity and at the same height above the ground. The Exotech radiometer was directed normal to the surface (zero view angle) of the panel and readings were recorded by alternately placing it over both the panels and noting the response. The readings were taken throughout the day to cover a range of zenith angles. The reference panel was considered azimuthally isotropic (Jackson *et al.*, 1987).

Standard reference panels have bi-directional properties that are represented by polynomials as a function of θ_z. Equation 3 is used to calculate the reflectance of the Halon panel ($R_{Halon}(0°/\theta_z)$) for different zenith angles recorded throughout the day. The $R_{Halon}(0°/\theta_z)$ is then substituted in Equation 2 to calculate the reflectance of $BaSO_4$ panel ($R_{BaSO4}(0°/\theta_z)$) for corresponding zenith angles

$$R_{Halon}(0°/\theta_z) = A0 + A1 * (\theta_z) + A2 * (\theta_z)^2 + A3 * (\theta_z)^3 + A4 * (\theta_z)^4 \quad (3)$$

where A0, A1, A2, A3, and A4 are known Halon panel coefficients from Table 1.

Zenith angle (θ_z) calculation

θ_z = f{CD, T_{st}, Lon_{st}, Lat_{loc}, Lon_{loc}, Solar time}

where, CD = Calendar day of the year; T_{st} = Local time; Lon_{st} = Standard longitude; Lat_{loc} = Local latitude; and Lon_{loc} = Local longitude.

The $R_{Halon}(0°/\theta_z)$ and $R_{BaSO4}(0°/\theta_z)$ values are plotted against zenith angle and a fourth order polynomial is fitted to the $BaSO_4$ reflectance curve. The coefficients of this polynomial are the coefficients A0, A1, A2, A3, and A4 of the $BaSO_4$ panel.

Panel Calibration Results

The Halon and $BaSO_4$ panel reflectance values in the Green, Red, and NIR bands are plotted against the corresponding zenith angles. Figure 8 shows the polynomial fitted to the $BaSO_4$ reflectance curves.

The bi-directional reflectance coefficients of $BaSO_4$ panel as obtained from the polynomials shown in Figure 8 are listed below in Table 2.

Table 2. Bi-directional Reflectance Coefficients of $BaSO_4$ Panel

$BaSO_4$ panel	A0	A1	A2	A3	A4
Red	-0.0685	0.1030	-0.0038	6.00E-05	-3.00E-07
Green	-1.3878	0.2041	-0.0066	9.00E-05	-5.00E-07
NIR	-2.1819	0.2794	-0.0092	1.00E-04	-7.00E-07

The following equations are used for calculating the reflectance value of the $BaSO_4$ reference panel in the Red, Green and NIR bands corresponding to any zenith angle:

$$R_{BaSO4, Red}(0°/\theta_z) = -0.0685 + 0.103(\theta_z) - 0.0038(\theta_z)^2 + 6E\text{-}05(\theta_z)^3 - 3E\text{-}07(\theta_z)^4 \quad (4)$$

$$R_{BaSO4, Green}(0°/\theta_z) = -1.3878 + 0.2041(\theta_z) - 0.0066(\theta_z)^2 + 9E\text{-}05(\theta_z)^3 - 5E\text{-}07(\theta_z)^4 \quad (5)$$

$$R_{BaSO4, NIR}(0°/\theta_z) = -2.1819 + 0.2794(\theta_z) - 0.0092(\theta_z)^2 + 0.0001(\theta_z)^3 - 7E\text{-}07(\theta_z)^4 \quad (6)$$

Calculation of $DN_R(t)$ - Panel Image Acquisition and Corrections Applied to Panel Images

While capturing panel images, the cameras are fitted with neutral density (ND) filters to reduce saturation of images due to brightness of the white panel. Also, there is a marked difference in brightness of the image at the periphery as compared to the center due to lens vignetting. Hence, the panel images are corrected for saturation and lens vignetting error.

Correction for Reference Panel Image Saturation

The saturated images of $BaSO_4$ panel had DN in the range of 250 to 255 inclusive. Hence, a neutral density (ND) filter was used on the camera with a fractional transmittance given by the following equation:

$$(I / I_0) = 10^{-d} \quad (7)$$

where, I is the measurable intensity, I_0 is the incident intensity, and d is the fractional transmittance. The fractional transmittance of the ND filters used on the camera is shown in Table 3.

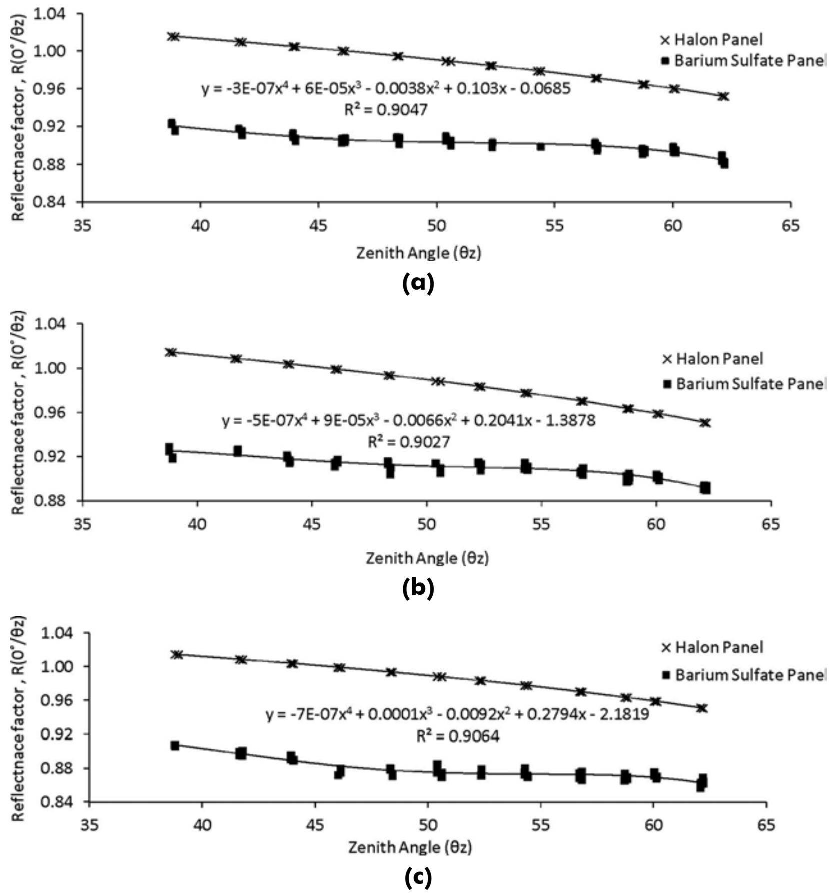

Figure 8. Panel cross calibration results showing coefficients of $BaSO_4$ panel: (a) Reflectance factor as a function of solar zenith angle for red band, (b) Reflectance factor as a function of solar zenith angle for Green band, and (c) Reflectance factor as a function of solar zenith angle for NIR band.

Table 3. Fractional Transmittance of Neutral Density Filters

Filter	Time	Fractional Transmittance			
		BLUE	GREEN	RED	NIR
0.3	1:39:00 PM (Before Flight)	50.25%	50.10%	50.10%	50.10%
0.4	2:15:00 PM (After Flight)	41.50%	41.75%	41.75%	42.25%

In this paper, the panel image ($DN_R(t)$) is called the corrected brightness value (CBV) after the ND filter effect is removed from panel image. The following section describes in detail the method adopted for producing the CBV in different bands.

Correction for Lens Vignetting

A normalized brightness value (NBV) is computed by averaging the DNs corresponding to the camera field of view (FOV) (Neale and Crowther, 1994). If there is some major shadowing, then center 20 × 20 pixels of the panel are averaged to obtain the NBV. The correction coefficient, $CC_{x,y(a,c,f)}$ for each aperture (a) /filter (f) /camera (c) combination is calculated using Equation 8. The CBV of the panel is computed using Equation 10, and it replaces $DN_R(t)$ in Equation 1. Figure 9 shows the model for CBV calculation.

$$CC_{x,y(a,c,f)} = \left(\frac{NBV_{(a,c,f)}}{BV_{x,y(a,c,f)}}\right) \tag{8}$$

where, CC is the correction coefficient for the x,y pixel; NBV is the image normalization brightness value; BV is the brightness value of pixel x,y; x = the pixel row; y = the pixel column; a = the aperture at which the image was acquired; c = the camera from which the image was acquired; and f= the neutral density filter under which the imagery was acquired.

To remove the effect of the ND filter from the reference panel images, the brightness values are divided by the transmittance factor (I/I_0) of the respective ND filter (Equation 9). This is to ensure that the calculation of reflectance value of the final images is not impacted, since the cameras on board the UAV do not have ND filters on them.

$$BV_{x,y(a,c,)} = BV_{x,y(a,c,f)} / (I/I_0) \tag{9}$$

$$CBV_{x,y(a,c)} = BV_{x,y(a,c)}. \tag{10}$$

A similar procedure is repeated for calculating the CBV of red, green, blue, and NIR channels for pre- and post-flight panel images. Then, the pre- and post-flight CBV of each band is averaged to get the final CBV for that band. Figure 10 shoes the lens vignetting effect and the applied correction.

AggieAir Image Reflectance Calculation Model - Conversion of UAV Digital Imagery, $DN_T(t)$ into Reflectance

The AggieAir acquired georeferenced, multispectral imagery of a section of the BRMBR on 17 June 2010. The flight time was about 30 minutes and the UAV was flown around local solar noon. The image footprints were first mosaicked and orthorectified. The mosaicked images were then processed to transform the DN into reflectance values using Equation 1. A model was prepared in ERDAS Imagine® for producing final reflectance images. The inputs to the model were reflectance of the

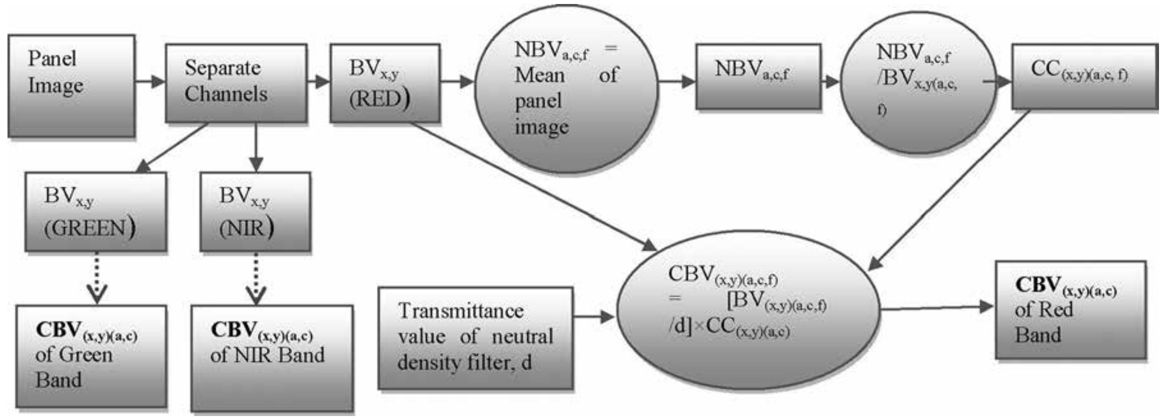

Figure 9. Model for calculation of CBV of the panel image in different bands.

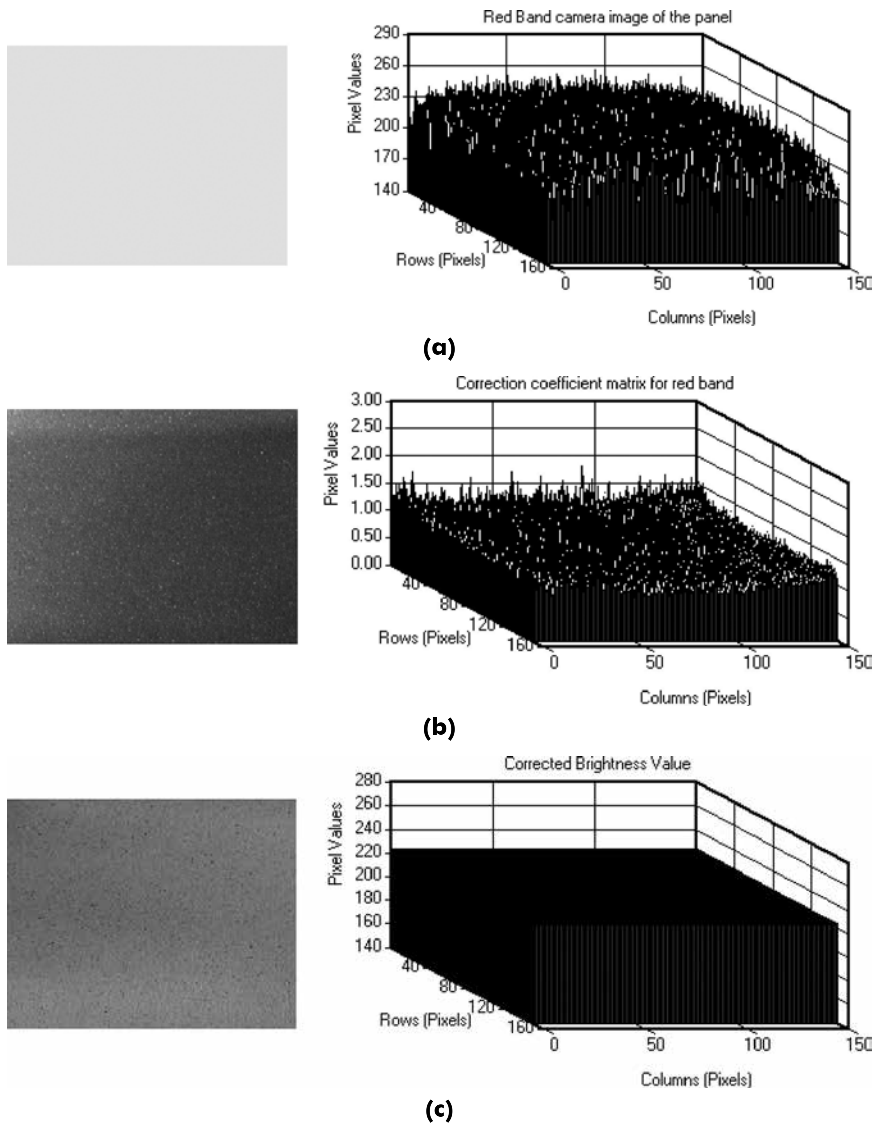

Figure 10. Correction for lens vignetting: (a) Panel image with lens vignetting effect at the edges, (b) Correction coefficient of the image, and (c) Corrected brightness value of the panel image.

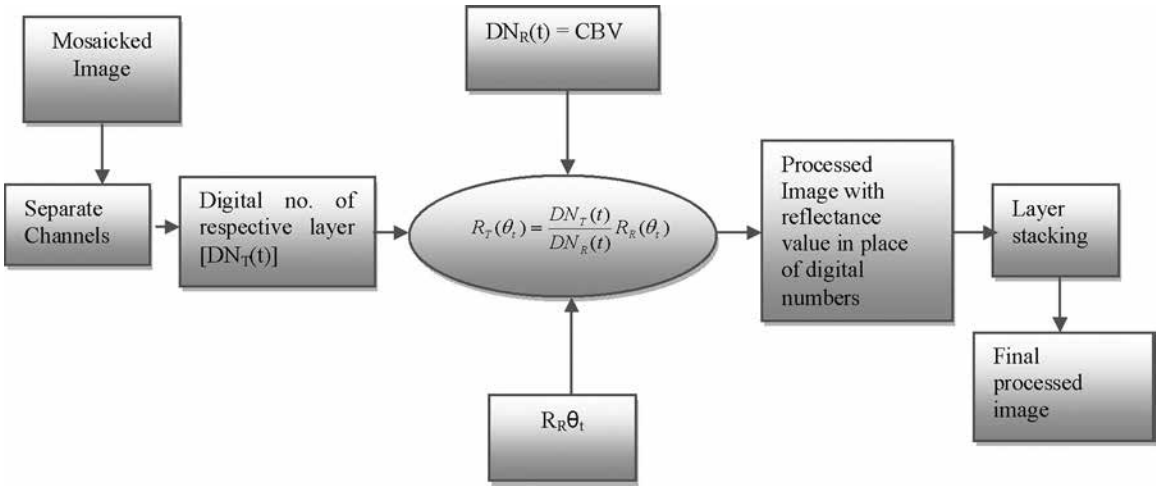

Figure 11. Model for calculation of reflectance of image.

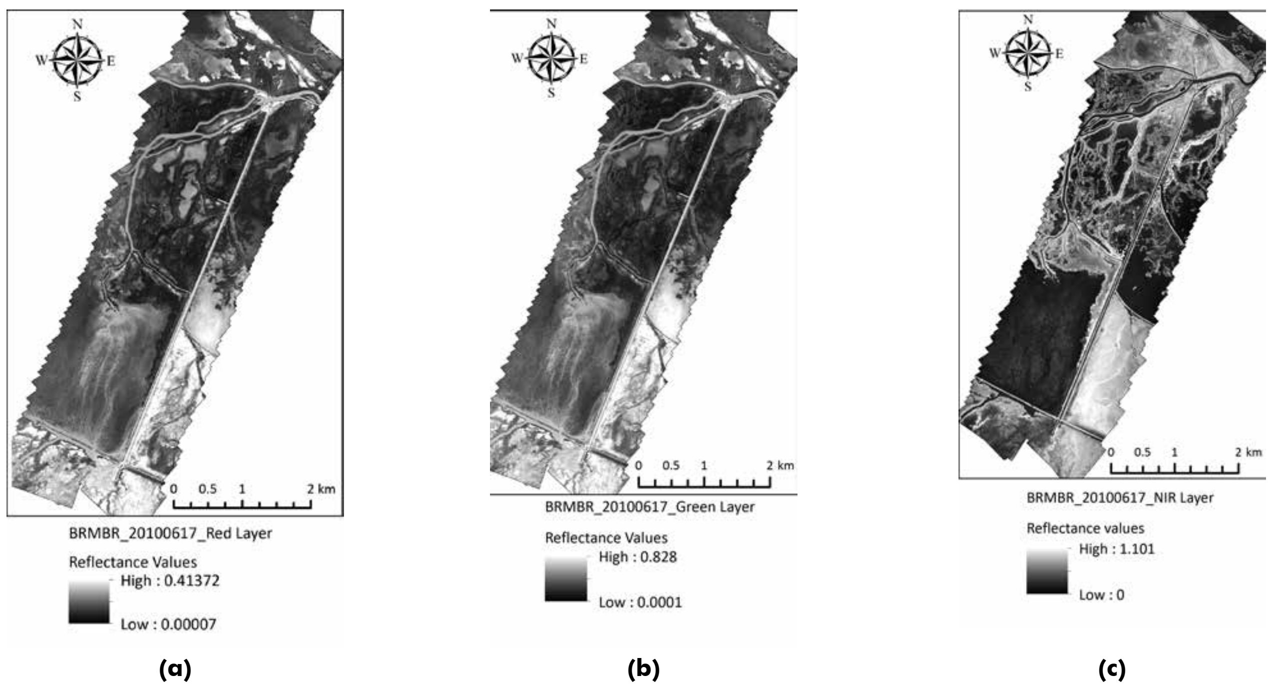

Figure 12. Red, Green, and NIR layers of the processed image.

reference panel, $R_{BaSO4}(0°/\theta_z)$ which was calculated using Equations 4, 5, and 6; the CBV of the reference panel corresponding to the day and time of image acquisition and brightness value of the imagery acquired by the UAV which is $DN_T(t)$.

The model for calculation of final reflectance values of the UAV digital imagery is shown in Figure 11. The mosaicked and orthorectified UAV imagery is delivered as input to the model. The model separates the image into Red, Green, and NIR channels. Each image array is divided by its respective CBV value, and then multiplied by the band specific reflectance factor of the reference panel. The outputs are individual Red, Green, and NIR layers with reflectance values in place of DN. These separate layers are then stacked together to produce the final image.

Results and Discussion

The goal of the research is to convert the raw imagery from the UAV AggieAir into reflectance images which have properties that are independent of changing irradiance and atmospheric conditions thus producing useful information from raw data. The model shown in Figure 11 produces processed reflectance image of the study area. In the last step of the model, the layers are stacked in such a way that the NIR is the top layer, beneath it is the green layer and Red as the bottom layer. While stacking one or more of image layers can be excluded from the stack and so chosen that the final image fulfills the research requirements. Figure 12 shows the different layers of the processed image as produced by the model.

When the DN values are converted to NIR reflectance values, there were pixels with reflectivity greater than 1. In Figure 12c, the maximum value of reflectance in the NIR band is

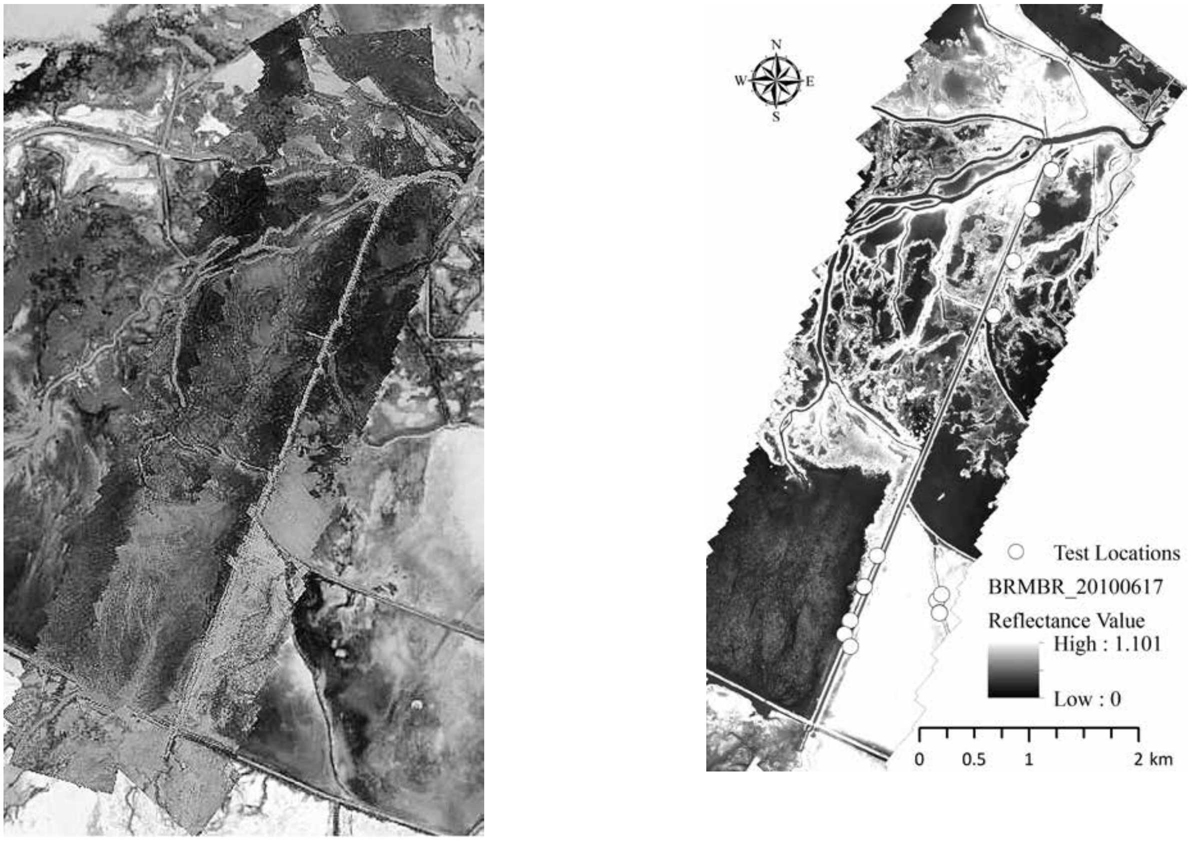

(a) (b)

Figure 13. Image to image comparison of raw imagery with final processed image: (a) Raw image tiles on a basemap, and (b) Final processed image.

Table 4. Reflectance Values in the NIR, Green, and Red Bands at Test Point Locations

ID	Latitude	Longitude	NIR	Green	Red	ID	Latitude	Longitude	NIR	Green	Red
1	392670	4589056	0.7546	0.6777	0.2853	11	393913	4591745	0.9692	0.2443	0.0859
2	392416	4588455	0.9618	0.5280	0.1994	12	393912	4591747	0.8841	0.2049	0.0756
3	392422	4588463	0.6400	0.5989	0.2166	13	393731	4591249	0.9248	0.2916	0.0756
4	392371	4588336	0.7250	0.4886	0.1719	14	393732	4591250	0.9174	0.3467	0.1306
5	392548	4588768	0.9988	0.7013	0.2510	15	392423	4588226	1.0580	0.8117	0.3610
6	392549	4588773	0.9877	0.4176	0.1478	16	393214	4588647	0.9914	0.4886	0.2338
7	394257	4592581	0.9507	0.4019	0.1306	17	393215	4588646	0.9840	0.4886	0.2406
8	394260	4592578	0.9803	0.2679	0.0997	18	393238	4588535	0.9100	0.3704	0.1513
9	394094	4592217	0.8360	0.3546	0.1341	19	393237	4588532	0.7731	0.4098	0.1409
10	394084	4592219	1.0173	0.2837	0.0859	20	393257	4588702	0.8915	0.4965	0.2269

1.101. This might happen if the reflected radiation somehow becomes greater than the measured incoming solar irradiance. The probable reasons might be (a) the nearby clouds and bright areas which might have increased the downwelling spectral irradiance on the surface objects which led to more upwelling radiation and higher spectral radiance going towards the UAV, and since reflectance factor is the ratio of outgoing to incoming radiation, this gets interpreted as being a larger reflectance value and sometimes a reflectance value greater than one; (b) the area has a lot of salt flats which might be acting as a source of specular reflection and the camera possibly measured the specular reflection along with scattered reflections; and (c) the sun and the measuring instrument were in the principal plane of the reflecting surface, and specular reflection was very strong which may have been the case since the measurements were taken around local solar noon. Since the precise and accurate measurement of reflectance factor is tedious task (Bartell *et al.*, 1980) and is unknown for many kinds of surface objects, it is quite possible to get estimated value for reflectance that is greater than unity.

Figure 13 shows an image to image comparison of the raw and processed data. Figure 13a shows raw image tiles from AggieAir shown on a basemap. Figure 13b shows the final processed orthorectified, mosaicked reflectance image of the study area. Imagery for an area as illustrated in Figure 12 and 13b, can be obtained in approximately one hour of flight time and the process of mosaicking and georeferencing such images requires from four to eight hours of processing (Zaman *et al.*, 2011). Thus, the calibration and image processing are executed in a timely manner. For comparison of processed data to field data, 20 locations from the 12 *Phragmites Australis* patches were chosen. The test locations are shown in figure 13b.

The reflectance values in the NIR, green, and red bands are extracted at the test locations by putting the latitude and longitude information in a GIS (Table 4). It is observed that the NIR values are consistently largest for all points with least values in the Red band. This agrees with the physical property of vegetation, and its response to electromagnetic radiation. In general, healthy vegetations are very good absorbers of electromagnetic energy in the visible region and reflectance in the blue and red regions are very low, with a slightly higher value in the green band. In the NIR band, absorption greatly reduces and spectral response of vegetation is much higher than in any portion of the visible spectrum.

Conclusions and Future Work

The study discusses the procedural workflow of processing and converting raw data obtained from a new UAV system AggieAir into reflectance values. Overall the results look good, and the reflectance values in the NIR, Red, and Green bands over vegetation test location points are consistent. *In situ* irradiance measurements and image measurements may not always be practicable in case of satellites but is possible with the UAVs. The reflectance values at test location indicated that the best results could be obtained by a combined adjustment of these simultaneous measurements and monitoring of radiance and irradiance conditions in the field.

It is assumed that the camera on board the UAV precisely records the radiance and is correct representation of upwelling radiance from the study area. However, the bright areas alter the optical path directed towards the camera, and it is possible for adjacency effects to raise the apparent reflectance values in the images. Other factors that affect luminance and image DN are camera related, such as vignetting, camera settings like international organization for standardization sensitivity value (ISO) and aperture, and color processing algorithms (Clemens, 2012). The inherent errors related to the aircraft sensors, i.e., the GPS, and IMU might result in some position errors in the images. Sensor payload restrictions for UAV and low altitude wide angle imagery contribute to Bayer filter interpolation and geometric errors to color imagery, respectively (Strecha *et al.*, 2012). The procedure presented in the paper is rigorous and has tried to rid the imagery of most of these errors. The described procedure is an effective means of UAV data processing and calibration and is successful in generating high quality images. Future development on this work will include a meaningful comparison of the AggieAir UAV data from time to time, site to site, and instrument to instrument.

Acknowledgments

This work was made possible by the generous funding and support of the Utah Water Research Laboratory (UWRL).The authors thank Mark Winkelaar for his help with GIS, Andrea Caroll and Jennnifer Fluckiger for help with the software, and Dr. Christopher Neale for his useful insights. The authors thank the anonymous reviewers for their constructive comments and recommendations, which greatly improved the quality of this article.

References

Bartell, F.O., E. Dereniak, and W. Wolfe,1980. The theory and measurement of bidirectional reflectance distribution function (BRDF) and bidirectional transmittance distribution function (BTDF), *Proceedings of SPIE 0257, Radiation Scattering in Optical Systems*, 03 March 1981, Vol. 154.

Berni, J., P. Zarco-Tejada, L. Suarez, V. Gonzalez-Dugo, and E. Fereres, 2009. Remote sensing of vegetation from UAV platforms using lightweight multispectral and thermal imaging sensors, *International Archives of Photogrammetry, Remote Sensing and Spatial Information Sciences*, Hannover, Germany, 38(1-4-7/W5).

Chao, H., Y. Cao, and Y. Chen, 2010. Autopilots for small unmanned aerial vehicles: A survey, *International Journal of Control, Automation and Systems*, 8:36–44.

Clemens, S.R., 2012. *Procedures for Correcting Digital Camera Imagery Acquired by the AggieAir Remote Sensing Platform*, MS thesis, Utah State University, Logan, Utah, 186 p.

Du, Q., N. Raksuntorn, A. Orduyilmaz, and L.M. Bruce, 2008. Automatic registration and mosaicking for airborne multispectral image sequences, *Photogrammetric Engineering & Remote Sensing*, 74(2):169–182.

Gates, D.M., 1980. *Biophysical Ecology*, Springer-Verlag, New York, 611 p.

Hakala, T., J. Suomalainen, and J.I. Peltoniemi, 2010. Acquisition of bidirectional reflectance factor dataset using a micro unmanned aerial vehicle and a consumer camera, *Remote Sensing*, 2(3):819–832.

Herwitz, S., L. Johnson, S. Dunagan, R. Higgins, D. Sullivan, J. Zheng, B. Lobitz, J. Leung, B.

Gallmeyer, and M. Aoyagi, 2004. Imaging from an unmanned aerial vehicle: agricultural surveillance and decision support, *Computers and Electronics in Agriculture*, 44(1):49– 61.

Hruska, R., J. Mitchell, M. Anderson, and N.F. Glenn, 2012. Radiometric and geometric analysis of hyperspectral imagery acquired from an unmanned aerial vehicle, *Remote Sensing*, 4(9):2736–2752.

Huang, C., B. Wylie, L. Yang, C. Homer, and G. Zylstra, 2002. Derivation of a tasselled cap transformation based on Landsat 7 at-satellite reflectance, *International Journal of Remote Sensing*, 23:1741–1748.

Hunt, Jr., E.R., M. Cavigelli, C.S. Daughtry, J.E. Mcmurtrey III, and C.L. Walthall,2005. Evaluation of digital photography from model aircraft for remote sensing of crop biomass and nitrogen status, *Precision Agriculture*, 6:359–378.

Hunt, E.R., W.D. Hively, S. Fujikawa, D. Linden, C.S. Daughtry, and G. McCarty, 2010. Acquisition of NIR-green-blue digital photographs from unmanned aircraft for crop monitoring, *Remote Sensing*, 2:290–305.

Jackson, R.D., M. Susan Moran, P.N. Slater, and S.F. Biggar, 1987. Field calibration of reference reflectance panels, *Remote Sensing of Environment*, 22(1):145–158.

Jackson, R.D., T.R. Clarke, and M. Susan Moran, 1992. Bidirectional calibration results for 11 spectralon and 16 $BaSO_4$ reference reflectance panels, *Remote Sensing of Environment*, 40:231–239.

Jensen, A.M., Y.Q. Chen, M. McKee, T. Hardy, and S.L. Barfuss, 2009. AggieAir - A low-cost autonomous multispectral remote sensing platform: New developments and applications, *Proceedings of the IEEE International Geoscience and Remote Sensing Symposium (IGARSS)*, Cape Town, South Africa, 12-17 July, pp. IV-995–IV-998.

Jensen, A.M., T. Hardy, M. McKee, and Y.Q. Chen, 2011. Using a multispectral autonomous unmanned aerial remote sensing platform (AggieAir) for riparian and wetlands applications, *Proceedings of the IEEE International Geoscience and Remote Sensing Symposium (IGARSS), 2011*, 24-29 July, Vancouver, Canada, pp. 3413–3416.

Laliberte, A., and A. Rango, 2008. Incorporation of texture, intensity, hue, and saturation for rangeland monitoring with unmanned aircraft imagery, *Proceedings of the International Archives of the Photogrammetry, Remote Sensing, and Spatial Information Sciences: GEOBIA 2008. Pixels, Objects, Intelligence*, 06-07 August, Calgary, Canada, 6 p.

Laliberte, A.S., and A. Rango,2009.Texture and scale in object-based analysis of subdecimeter resolution unmanned aerial vehicle (UAV) imagery, *IEEE Transactions on Geoscience and Remote Sensing*, 47:761–770.

Laliberte, A.S., M.A. Goforth, C.M. Steele, and A. Rango, 2011. Multispectral remote sensing from unmanned aircraft: Image processing workflows and applications for rangeland environments, *Remote Sensing*, 3(11):2529–2551.

Lebourgeois, V., S. Labbe, F.D.R. Jacob, and A. Begue 2008. Atmospheric corrections of low altitude thermal infrared airborne images acquired over a tropical cropped area, *IEEE International Geoscience and Remote Sensing Symposium*, 06-11 July 6-11, Boston, Massachusetts, pp. 672–675.

Miura, T., and A.R. Huete, 2009. Performance of three reflectance calibration methods for airborne hyperspectral spectrometer data, *Sensors*, 9(2):794–813.

Moran, M., R. Bryant, K. Thome, W. Ni, Y. Nouvellon, M. Gonzalez-Dugo, J. Qui, and T.R. Clarke, 2001. A refined empirical line approach for reflectance factor retrieval from Landsat-5 TM and Landsat-7 ETM+, *Remote Sensing of Environment*, 78(2001):71–82.

Neale, C.M., and B.G. Crowther, 1994. An airborne multispectral video/radiometer remote sensing system: Development and calibration, *Remote Sensing of Environment*, 49(3):187–194.

Nicodemus, F.E., J.C. Richmond, and J.J. Hisa, 1977. Geometrical considerations and nomenclature for reflectance, *NBS Monograph 160*, National Bureau of Standards, Washington, D. C.

Primicerio, J., S.F. Di Gennaro, E. Fiorillo, L. Genesio, E. Lugato, A. Matese, and F.P. Vaccari, 2012. A flexible unmanned aerial vehicle for precision agriculture, *Precision Agriculture*, 13(4):517–523.

Robinson, B., and L. Biehl, 1979. *Calibration Procedures for Measurement of Reflectance Factor in Remote Sensing Field Research*, Society of Photo-Optical Instrumentation Engineers, 196:16–26.

Sheng, H., H. Chao, C. Coopmans, J. Han, M. McKee, and Y. Chen, 2010. Low-cost UAV-based thermal infrared remote sensing: Platform, calibration and applications, *IEEE/ASME International Conference on Mechatronics and Embedded Systems and Applications (MESA)*, 15-17 July, Qingdao, Shan Dong, China, pp. 38–43.

Strecha, C., A. Fletcher, A. Lechner, P. Erskine, and P. Fua, P., 2012. Developing species specific vegetation maps using multi-spectral hyperspatial imagery from unmanned aerial vehicles, *ISPRS Annals of Photogrammetry, Remote Sensing and Spatial Information Science*, 25 August-01 September, Melbourne, Victoria, Australia, pp. 311–316.

Watts, A.C., V.G. Ambrosia, and E.A. Hinkley, 2012. Unmanned aircraft systems in remote sensing and scientific research: Classification and considerations of use, *Remote Sensing*, 4:1671–1692.

Wilkinson, B.E., B.A. Dewitt, A.C. Watts, A. H. Mohamed, and M.A. Burgess, 2009. A new approach for pass-point generation from aerial video imagery, *Photogrammetric Engineering & Remote Sensing*, 75(12):1415–1423.

Zaman, B., A.M. Jensen, and M. McKee, 2011. Use of high-resolution multispectral imagery acquired with an autonomous unmanned aerial vehicle to quantify the spread of an invasive wetlands species, *Proceedings of the IEEE International Geoscience and Remote Sensing Symposium (IGARSS)*, 24-29 July, Vancouver, Canada, pp. 803–806.

Zhang, C., J.M. Kovacs, 2012. The application of small unmanned aerial systems for precision agriculture: A review, *Precision Agriculture*, 13(6):693–712.